Thin Solid Films 603 (2016) 334–341

Contents lists available at ScienceDirect

Thin Solid Films

journal homepage: www.elsevier.com/locate/tsf

Infrared optical responses of wurtzite $In_xGa_{1-x}N$ thin films with porous surface morphology

P. Yew [a,b,*], S.C. Lee [b,c], S.S. Ng [a], H. Abu Hassan [b], W.L. Chen [d], T. Osipowicz [e], M.Q. Ren [e]

[a] Institute of Nano-Optoelectronics Research and Technology (INOR), Universiti Sains Malaysia, 11800 Minden, Penang, Malaysia
[b] School of Physics, Universiti Sains Malaysia, 11800 Minden, Penang, Malaysia
[c] Centre of Excellence for Pre-University Studies, INTI International College Penang, Laureate International University, 1-Z, Lebuh Bukit Jambul, 11900 Penang, Malaysia
[d] Department of Electronic Engineering, National Changhua University of Education, 500, Taiwan, ROC
[e] Centre for Ion Beam Applications (CIBA), Department of Physics, National University of Singapore, Singapore 119260, Singapore

ARTICLE INFO

Article history:
Received 28 May 2015
Received in revised form 25 January 2016
Accepted 22 February 2016
Available online 24 February 2016

Keywords:
Optical phonon modes
Wurtzite InGaN
Porous
LPP
Phonon mode shift

ABSTRACT

Room temperature infrared (IR) optical responses of wurtzite indium gallium nitride ($In_xGa_{1-x}N$) in the composition range of $0.174 \le x \le 0.883$ were investigated by the polarized IR reflectance spectroscopy. Analyses of the amplitudes of oscillation fringes in the non-reststrahlen region revealed that the high frequency dielectric constants of the samples were unusually smaller than the values predicted from the Clausius–Mossotti relation. This odd behavior was attributed to the porous surface morphology of the $In_xGa_{1-x}N$ samples. The E_1 optical phonon modes of the $In_xGa_{1-x}N$ were deduced from the composition dependent reststrahlen features. The obtained values were compared to those calculated through the modified random element iso-displacement (MREI) model. The deviation between the measured data and the MREI model prediction were explained in detail from the aspects of strain, thermal expansion and anharmonic phonon-coupling. Finally, it was found that the large discrepancy of the E_1(LO) mode is mainly attributed to the effects of the longitudinal phonon–plasmon coupling.

1. Introduction

In year 2014, the Nobel Prize in Physics was awarded jointly to Isamu Akasaki, Hiroshi Amano and Shuji Nakamura for the invention of efficient blue light-emitting diodes [1]. One of the key materials for these light-emitting diodes (LEDs) is indium gallium nitride (InGaN). Despite the energy efficient solid-state LEDs products already available on the market, issues concerning its growth conditions and material properties still remain a controversial matter and are a subject of an ongoing debate in the literature. Apart from lighting applications, few investigations revealed that the role of optical phonon in thermal conductivity can no longer be ignored especially in nanostructures [2,3]. Hot phonon effect and phonon bottleneck effect resulted from the electron–phonon interaction can severely affect the electron mobility and electrical conductivity of high speed electronic devices [4]. As all these properties are closely associated to the performance and efficiency of devices, the interpretation of optical phonon modes for wurtzite structure InGaN have been extensively studied for realization of various related optoelectronic devices.

At Brillouin zone center, the optical phonon branches for a wurtzite structure crystal are constituted of A_1 (parallel to the optic axis (*c*-axis)), E_1 (perpendicular to the *c*-axis), E_2 and B_1 (silent) modes. B_1 is neither infrared (IR)-active nor Raman-active. The non-polar E_2 is Raman-active; the remaining polar A_1 and E_1 are both Raman-active and IR-active. Among all the optical phonon branches, A_1(LO) and E_2 modes of wurtzite InGaN were mostly studied by means of Raman spectroscopy [5–10] and spectroscopic ellipsometry [11]. Very few attempts have hitherto been made to study E_1 optical vibrational components of InGaN [11–13]. In addition, the characterization is very limited to Ga-rich InGaN alloys [11,12,14]. Hence, it is essential to investigate E_1 phonon modes of InGaN with different crystalline qualities and structural properties for metrology purpose and further investigations of its heterostructure properties.

Longitudinal optical (LO) phonon–plasmon coupling (LOPC) is the interaction between the electric dipole moment due to the relative displacement of the ions and the electric field associated with free carriers [15]. The LOPC gives rise to coupled modes, namely longitudinal phonon–plasmon (LPP) modes which are directly observable in Raman and IR spectroscopic measurements. Numerous theoretical [16] and experimental [17–21] investigations have been established to study the properties of coupled mode in doped semiconductors. To date, only little work has been done on A_1 LPP [6,9] and E_1 LPP [22] modes of wurtzite InGaN. Because of the surface Fermi level of $In_xGa_{1-x}N$, particularly with In content larger than 43%, is pinned above the charge neutrality level [23,24], unintentionally-doped InGaN typically exhibits

* Corresponding author.
E-mail address: paulinevcu@hotmail.com (P. Yew).

http://dx.doi.org/10.1016/j.tsf.2016.02.039
0040-6090/

high free carrier concentration. Determination of LO phonon mode of InGaN is generally difficult because the spectral feature is not induced by LO individually but the LPP modes.

The optical properties of a material can be greatly changed by surface morphology [25,26]. Several profound characteristics of porous structure, for instance, increase of total surface area, enhanced photoluminescence effect, an offer of a better epitaxial growth template and etc., have successfully make porous semiconductors become a hot research topic [25–27]. For example, porosity induces an additional TO–LO mode pair ($\omega_{TO,F}$–$\omega_{LO,F}$), so-called Fröhlich modes. The Fröhlich modes lie in between the gap of TO and LO vibrational frequency of flat semiconductor (i.e., $\omega_{TO} \le \omega_{LO,F} \le \omega_{TO,F} \le \omega_{LO}$) [28]. Moreover, carrier concentration profile has been related to porous morphology [29–31]. Look et al. emphasized that the pore surface which acts as electron traps is the major factor for the drop of carrier concentration in anodized SiC [30].

In this work, the room temperature IR optical properties of *c*-plane oriented wurtzite $In_xGa_{1-x}N$ ($0.174 \le x \le 0.883$) thin films with porous surface morphology were investigated by Fourier transform IR (FTIR) reflectance spectroscopy. A multi-oscillator dielectric function model was employed to analyze the spectral features. The relationship between the high frequency dielectric constant and the porous surface morphology of the samples was investigated with the aid of effective medium theory. Subsequently, we employed modified random element iso-displacement (MREI) model to predict the harmonic E_1 optical phonon modes in long wavelength limit. Instead of the uncoupled E_1 (LO) mode, the LPP modes of wurtzite $In_xGa_{1-x}N$ which arise from LOPC were reported. Finally, possible factors that account for the deviation between the theoretical predictions and measured optical phonon modes were discussed.

2. Experiment details

Four commercial unintentionally doped n-type $In_xGa_{1-x}N$ thin films with *c*-plane orientation were used in this study. The as-received $In_xGa_{1-x}N$ thin films were grown by molecular beam epitaxy on top of sapphire (Al_2O_3) substrate with a very thin AlN buffer layer (~20 nm). Proton induced X-ray emission (PIXE) was used to determine the In/Ga ratio. The measurements were carried out at the Centre for Ion Beam Applications (CIBA) at the National University of Singapore (NUS), Singapore. A 2 MeV proton beam under 45° to the sample normal (SN) was used in combination with a Si(Li) detector, also under 45° to the SN. From the intensity of the In L and the Ga K X-rays, the atomic ratio of Ga to In was derived, using the empirically known X-ray production cross sections [32]. The composition of the four wurtzite $In_xGa_{1-x}N$ thin films was determined as $x = 0.174$, 0.477, 0.719, and 0.883. To ease the discussion, the samples were labeled as InGaN20, InGaN40, InGaN60 and InGaN80 for $x = 0.174$, 0.477, 0.719, and 0.883, respectively. The lattice constants a_L and c_L of the films were determined by X-ray diffraction reciprocal space mapping (RSM) technique (model: Siemens D5000 spectrometer). The *c*-plane wurtzite $In_xGa_{1-x}N$ thin films experience biaxial stress $\sigma_{xx} = \sigma_{yy}$ and vanished uniaxial stress $\sigma_{zz} = 0$ [33]. The strain states of $In_xGa_{1-x}N$ thin film, i.e., out-of plane strain, $\epsilon_{zz} = (c_L - c_L^R) / c_L^R$ and the in-plane strain, $\epsilon_{xx} = \epsilon_{yy} = (a_L - a_L^R) / a_L^R$ were calculated. Subsequently, surface morphology and cross section of the samples were studied by means of field emission scanning electron microscopy (FESEM, FEI Nova NanoSEM 450).

Room temperature *s*-polarized IR (400–7800 cm^{-1}) reflectance measurements were performed on wurtzite $In_xGa_{1-x}N$ samples using a FTIR spectrometer (Spectrum GX FTIR, Perkin Elmer) with the aid of a thallium iodide bromide polarizer. All the measurements were carried out at incident angle of 16° with the aid of a Perkin Elmer fixed angle (16°) specular reflectance accessory. An aluminium coating mirror was used as reference standard. Note that "*s*-polarized" means that the electric field of the incident light beam is polarized perpendicular to the surface normal of the sample, where the surface normal is parallel to the *c*-axis. Under the *s*-polarized configuration, the E_1 optical phonon modes can be excited effectively.

3. Theory

The IR reflectance spectra of vacuum/$In_xGa_{1-x}N$/AlN/Al_2O_3 heterostructures were simulated by using standard multi-layer optics technique [34]. The least-squares curve fitting technique was used to extract the parameters from the reflectance spectra. Dielectric function $\varepsilon(\omega)$ and thickness *d* of each layer in the heterostructures are two indispensable parameters for the simulation. Unlike zincblende phase, wurtzite alloys possess directional dependence of optical phonon modes i.e., A_1 modes and E_1 modes due to the anisotropy which is stemmed from the short range inter-atomic force. Thus, the effects of anisotropy must be taken into account in examining the dielectric function of uniaxial crystal. Assume that the *c*-axis is parallel to the crystal surface normal (*c*-axis || *z*) and perpendicular to the direction of wave propagation (*c*-axis ⊥ *x*), the dielectric function is given by [35,36]:

$$\varepsilon_{\perp}(\omega) = \varepsilon_{\infty,\perp}\prod_{j}^{N}\left(\frac{\omega_{LOj}^2-\omega^2-i\omega\gamma_{LOj}}{\omega_{TOj}^2-\omega^2-i\omega\gamma_{TOj}}\right)_{\perp} - \left(\frac{\varepsilon_{\infty}\omega_p^2}{\omega\left(\omega+i\gamma_p\right)}\right)_{\perp}, \quad (1)$$

where ω, ε_∞, ω_{TO}, ω_{LO} and γ are the angular frequency, high frequency dielectric constant, transverse optical (TO), longitudinal optical (LO) phonon modes, and damping constant, respectively. The subscript *N* and *j* represent the total number of phonon oscillators and specific number of oscillator, respectively. The second term descends from the consideration of plasmon (free carrier) and ω_p represents the plasmon frequency. Eq. (1) assumed that the contributions of phonon and plasmon are independent and additive. As the damping of Eq. (1) is neglected and using the relation $\varepsilon_\infty(\omega) = 0$, $\omega_{LPP\pm}$ can be related to unscreened ω_{LO} analytically as follow:

$$\omega_{LPP\pm,\perp}^2 = \frac{1}{2}\left[\left(\omega_p^2+\omega_{LO}^2\right) \pm \sqrt{\left(\omega_p^2+\omega_{LO}^2\right)^2 - 4\omega_p^2\omega_{TO}^2}\right]_{\perp}. \quad (2)$$

Note that the plasmon frequency (ω_p) and plasmon damping (γ_p) are related to carrier concentration (*n*) and the mobility (μ), respectively by Drude approximation, i.e., $\omega_p^2 = ne^2 / (\varepsilon_o\varepsilon_\infty m^*)$ and $\gamma_p = e / (m^*\mu)$ [37] The symbols ε_o, m^* and *e* denote the permittivity in free space, effective mass and electron charge, respectively.

Aforementioned, the Coulomb interaction between the free carriers and LO phonons gives rise to insensitivity in probing the plasmon and LO phonon modes separately. Hence, it is more appropriate to employ Kukharskii extended generalized Lyddane–Sachs–Teller dielectric model ($\varepsilon_\perp^k$) which take account of LOPC to describe the optical properties of doped semiconductors [21,38,39]. Specifically, the general form of factorized dielectric model for polar semiconductor with two coupled modes, i.e. ω_{LPP+} and ω_{LPP-} can be expressed as follows [38]:

$$\varepsilon_{\perp}^k(\omega) = \left[\varepsilon_{\infty}\frac{\left(\omega^2-\omega_{LPP_+}^2+i\omega\gamma_{LPP_+}\right)\left(\omega^2-\omega_{LPP_-}^2+i\omega\gamma_{LPP_-}\right)}{\omega\left(\omega+i\gamma_p^k\right)\left(\omega^2-\omega_{TO}^2+i\omega\gamma_{TO}\right)}\right]_{\perp}. \quad (3)$$

Eq. (3) is only valid for the system with single lattice oscillator ($j = 1$). Under the circumstance of small damping, plasmon frequency of $\varepsilon_\perp^k$ (i.e., $\omega_p^k = \omega_{LPP+}\omega_{LPP-} / \omega_{TO}$) can be retrieved from Eq. (3) [38,39].

MREI [40,41] model has been recognized as a successful model to predict the optical phonon harmonic frequency of ternary mixed crystal. By following the procedure as demonstrated in Refs. [41,42], $\omega_{TO,MREI}$ and $\omega_{LO,MREI}$ of wurtzite $In_xGa_{1-x}N$ in the long wavelength limit ($k \sim 0$) can be determined by substituting the local electric field E_{loc}

with $E_{loc} = E + (4\pi / 3)g_iP$. E is the macroscopic electric field and P is polarization field. The ideal wurtzite structure constant g_i is included in the E_{loc} to consider the anisotropy of uniaxial structure i.e., $g_\perp = 1 + 0.2(3 / 4\pi)$ and $g_\parallel = 1 - 0.1(3 / 4\pi)$, respectively [43]. In this study, only $g_\perp$ is considered.

The required input parameters in MREI model are $\varepsilon_{\infty,GaN(InN)} = 5.2(8.4)$, $\omega_{TO,GaN(InN)} = 559(476)\ cm^{-1}$, $\omega_{LO,GaN(InN)} = 741(593)\ cm^{-1}$, respectively. We used lattice constants ${a_{GaN(InN)}}^R = 3.1890(3.5378)$ Å and ${c_{GaN(InN)}}^R = 5.1855(5.7033)$ Å as the unstrained lattice values throughout this work [44–48]. It is worth mentioning that wurtzite $In_xGa_{1-x}N$ exhibits one-mode behavior for composition dependence of both A_1 and E_1 optical phonon modes [42,49]. The $\omega_{TO,MREI}$ and $\omega_{LO,MREI}$ predicted from the MREI model were used as initial guesses in the curve fitting procedure for the $In_xGa_{1-x}N$ thin films.

The wavelength of the IR radiation is much larger than the structure dimension. In such quasi-static limit, the optical properties of the heterogeneous system i.e., mixtures of air and InGaN thin film can be treated by uniform effective medium theory (EMT). Within small applicability range where volume fraction of inclusion, $f \le 1/3$ [50], non self-consistent Maxwell Garnett (MG) approach is used in analyzing the effective dielectric properties of the composite material. Assume that the cylindrical air filled pores along *z* direction (parallel to the *c*-axis), the interface layers of the material lie on the *xy* plane (perpendicular to *c*-axis) and under the framework of MG type on cylindrical geometry, the birefringence effects give the effective uniaxial dielectric properties (depolarization factor, $L_i = 0.5$) in E_1 direction as follow [28,51]:

$$\frac{\tilde{\varepsilon}_\perp - \varepsilon_h}{\tilde{\varepsilon}_\perp + \varepsilon_h} = f_i \frac{\varepsilon_i - \varepsilon_h}{\varepsilon_i + \varepsilon_h}, \tag{8a}$$

$$f_i = \left(\frac{\tilde{\varepsilon}_{\infty,\perp} - \varepsilon_{\infty,h}}{\tilde{\varepsilon}_{\infty,\perp} + \varepsilon_{\infty,h}}\right)\left(\frac{\varepsilon_{\infty,i} + \varepsilon_{\infty,h}}{\varepsilon_{\infty,i} - \varepsilon_{\infty,h}}\right). \tag{8b}$$

$\tilde{\varepsilon}_\perp$ is the dielectric functions of effective medium. The subscripts h and i represent the host material and air inclusion, respectively. f_i is the volume concentration of air cavity (porosity) and $\sum f_i = 1$. With the same assumption on microstructural geometry ($L_i = 0.5$), self-consistent Bruggeman (BR) theory gives [52]:

$$f_1 \frac{\varepsilon_1 - \tilde{\varepsilon}_\perp}{\varepsilon_1 + \tilde{\varepsilon}_\perp} + f_2 \frac{\varepsilon_2 - \tilde{\varepsilon}_\perp}{\varepsilon_2 + \tilde{\varepsilon}_\perp} = 0, \tag{9a}$$

$$f_1 = \frac{(\varepsilon_{\infty,1} + \tilde{\varepsilon}_{\infty,\perp})(\varepsilon_{\infty,2} - \tilde{\varepsilon}_{\infty,\perp})}{(\varepsilon_{\infty,1} - \tilde{\varepsilon}_{\infty,\perp})(\varepsilon_{\infty,2} + \tilde{\varepsilon}_{\infty,\perp}) + (\varepsilon_{\infty,1} + \tilde{\varepsilon}_{\infty,\perp})(\varepsilon_{\infty,2} - \tilde{\varepsilon}_{\infty,\perp})}, \tag{9b}$$

where f_1 (f_2) is the volume fraction of constituent material with ε_1 (ε_2). Here, $\varepsilon_{\infty,1} = 1$ and f_1 is the air porosity. The subscript 2 denotes to the host material, i.e., $In_xGa_{1-x}N$. The Eqs. (9a) and (9b) are applicable in the range of $0 \le f_1 \le 1$ but limited for $0.05 < |\varepsilon_2(\omega) / \varepsilon_1(\omega)| < 20$ [53]. By having the best-fit high frequency dielectric constant, namely $\varepsilon_{\infty,IR}$ as standard reference, the porosity can be calculated by using the Eqs. (8b) and (9b).

4. Results and discussion

Using the relaxed lattice parameters of InN and GaN, ε_∞ of the mixed crystal $In_xGa_{1-x}N$ can be calculated based on the Clausius–Mossotti (CM) expression as below [41]:

$$\frac{\varepsilon_\infty - 1}{\varepsilon_\infty + 2} = (1-x)\left(\frac{V_{GaN}}{V}\right)\left(\frac{\varepsilon_{\infty,GaN} - 1}{\varepsilon_{\infty,GaN} + 2}\right) + x\left(\frac{V_{InN}}{V}\right)\left(\frac{\varepsilon_{\infty,InN} - 1}{\varepsilon_{\infty,InN} + 2}\right). \tag{10}$$

The symbol *V* refers to the intermediate volume of unit cell for the mixed crystal InGaN with particular composition, x respectively. The obtained $\varepsilon_{\infty,CM}$ values were used to simulate the theoretical

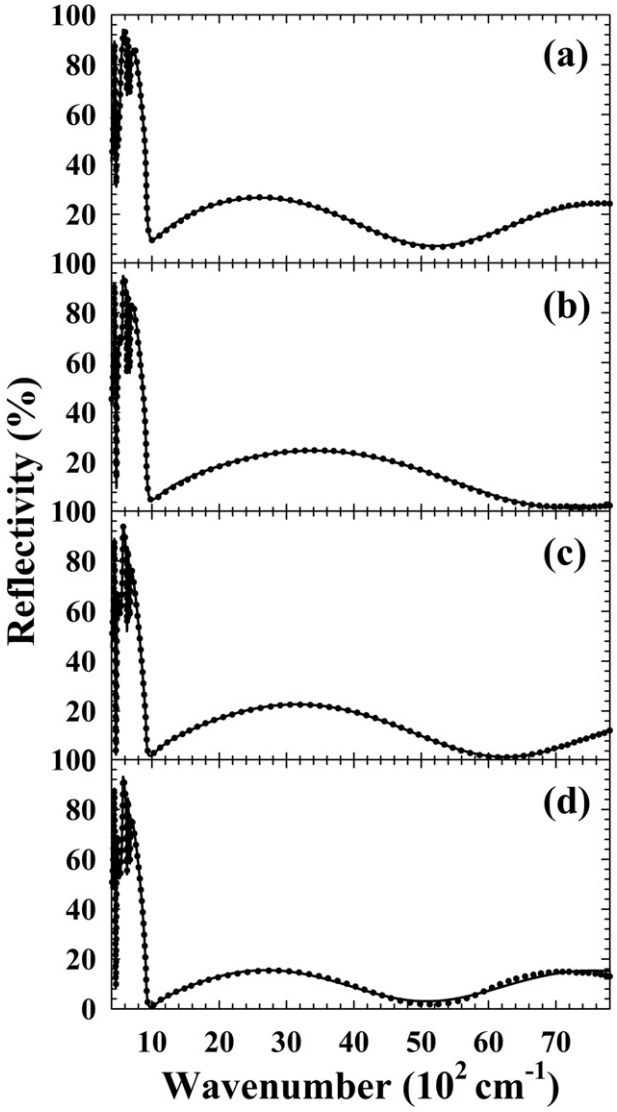

Fig. 1. Non reststrahlen region of s-polarized IR spectra for wurtzite structure $In_xGa_{1-x}N$ with (a) x = 0.174, (b) x = 0.477, (c) x = 0.719 and (d) x = 0.883. The dotted (solid) lines refer to experimental (calculated) data.

s-polarized IR reflectance spectra for wurtzite structure $In_xGa_{1-x}N$ with x = 0.174, 0.477, 0.719 and 0.883.

Fig. 1 shows the measured room temperature *s*-polarized IR reflectance spectra for wurtzite structure $In_xGa_{1-x}N$ with x = 0.174, 0.477, 0.719 and 0.883. The spectral responses from ~1000 to 7800 cm^{-1} (non-reststrahlen region) are sensitive to $\varepsilon_{\infty,IR}$ and *d*. By fitting the theoretical spectra to the experimental data, $\varepsilon_{\infty,IR}$ and *d* can be extracted. Through curve fitting analysis, we found that the assumption of single layer of InGaN thin film in the model structure gives a poor agreement between the experimental and theoretical spectra. Meanwhile, the $\varepsilon_{\infty,IR}$ of $In_xGa_{1-x}N$ layers are significantly lower than that of the usual prediction of CM relation, especially with the increasing of x. The decrement of ε_∞ ($\Delta\varepsilon_\infty = \varepsilon_{\infty,CM} - \varepsilon_{\infty,IR}$) is deduced as the consequence of existence of void component [54], which is related to the porosity of the $In_xGa_{1-x}N$ (will be discussed later). To verify this statement, the surface morphology and cross-section of the samples were investigated by FESEM measurements. As seen in Figs. 2 and 3, all InGaN thin films exhibit significant porous surface morphologies and air cavities. We believe that the porous surface morphologies of the as-received $In_xGa_{1-x}N$ samples is most likely caused by the III/V precursor ratio uses during the growth [54]. The air component (where $\varepsilon_\infty = 1$) plays the most critical role in reducing the dielectric constant of the

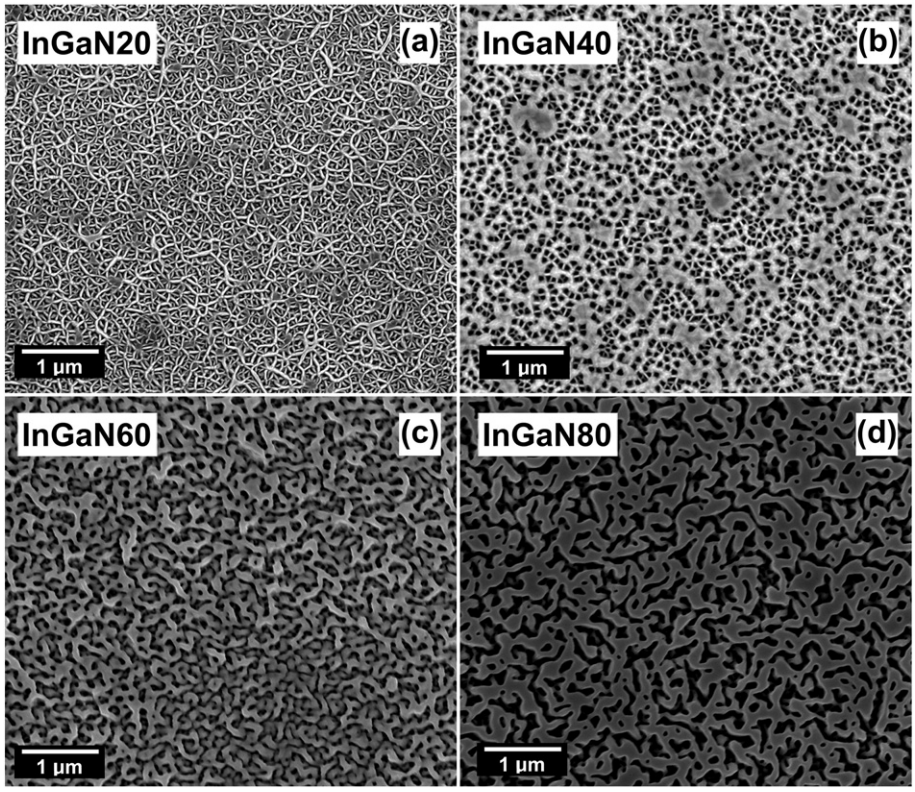

Fig. 2. FESEM surface measurements (top view) of (a) InGaN20, (b) InGaN40, (c) InGaN60 and (d) InGaN80.

$In_xGa_{1-x}N$ thin film. The amount of the air pores in the thin film is responsible for the deviation between the CM calculated and the fitted values of ε_∞, i.e., $\Delta\varepsilon_\infty$ increases with the porosity.

To further clarify the porous morphology of the samples, FESEM images were taken at tilted angles, as shown in the inset pictures in Fig. 3. It is clear that for each sample, the porosity is higher at the sample

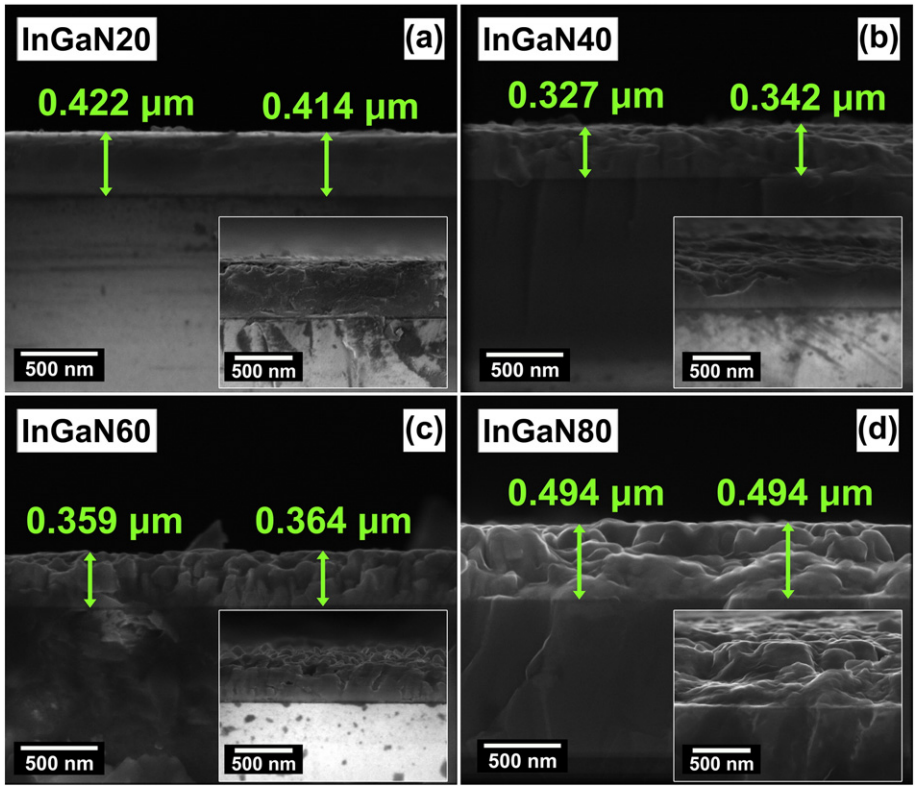

Fig. 3. FESEM cross-sectional images of (a) InGaN20, (b) InGaN40, (c) InGaN60 and (d) InGaN80. Inset figures display the FESEM images taken at tilted angles.

surface whereas, the porosity is lower at the region away from the sample surface. Hence, we proposed a template consisting of two porous layers with different ε_∞ for each of the $In_xGa_{1-x}N$ thin films in the spectra fitting procedure. Here, the top layer and the bottom layer of $In_xGa_{1-x}N$ are denoted as L1 and L2, respectively. Based on this assumption, excellent agreement between the calculated and the experimental spectra was obtained, as shown in Fig. 1. The fitting parameters for non-reststrahlen region were tabulated in Table 1. The total thickness of these two porous layers (i.e., $d_{L1} + d_{L2}$) agrees well with the measured thickness from FESEM as detailed in Fig. 3 for all $In_xGa_{1-x}N$ thin films.

MG and BR models were applied to quantitatively investigate the porosity of the samples, as shown in Fig. 4. Consistent to the FESEM images, model analyses of MG and BR showed that the top layer (L1) is less packed than the bottom layer (L2) for all the samples. The results also revealed that L1 in all samples possesses large volume fraction of air which exceeds the MG model limit (i.e., $f \le 1/3$) except for InGaN20 which has low porosity for both layers. Conversely, L2 of all the samples satisfy the validity of MG model. On the other hand, the necessary condition of BR model is satisfied as well for both of the layers in all the samples. Note that the difference between the BR and MG calculated porosity increases with volume fraction of air.

The mentioned procedures used in porosity calculation are only able to provide a fair estimation. To achieve better result, distinct depolarization factors which account for different geometrical structures should be considered. Generally, the EMT predicted parameters are highly dependent on selected topology [52], microstructural geometry [55] and self-consistency [56]. Spanier and Herman suggested that a hybrid model of phenomenological and spectral density functions dielectric functions can yield the superior results than the mere phenomenological model [57]. However, among all the commonly used effective medium theories, MG and BR are exploited due to their simplicity. In Refs. [56,57], better qualitative agreement with experiments given by MG approach was claimed. Nonetheless, the authentic porosity is believed lies in between the self-consistent and non self-consistent theories limit [52].

We turn to discuss the resonant reststrahlen band properties of wurtzite $In_xGa_{1-x}N$ alloys. Fig. 5 shows the experimental IR reflectance spectra of $In_xGa_{1-x}N$ samples as well as the simulated air/sapphire and air/AlN/sapphire IR reflectance spectra. Compared to the bare sapphire spectrum, the dip which originates from AlN can be clearly observed at $\omega \approx 675\ cm^{-1}$ (region II). Composition dependence of optical phonon mode for the samples can also be easily identified from the shaded region with horizontal lines (region I), which has high sensitivity to probe TO mode. The shaded region with slanted lines (region III) showed the distortion of spectral features, which are sensitive to the LPP modes and their damping.

Curve fitting of the *s*-polarized IR reflectance spectra of each sample are presented in Fig. 6. To visualize the phonon resonances clearly, the corresponding first derivative (FD) calculation of the spectra are also performed. Excellent agreement between the calculated spectra and measured spectra is achieved. In the fitting procedure, ω_{TO} and ω_{LO} are treated as finger-print properties. Hence, we assumed that ω_{TO} and ω_{LO} are identical for both of the upper and lower porous layers of $In_xGa_{1-x}N$ thin film. Through acquire the best-fit of experimental spectra, $\omega_{TO,IR}$, LPP+, LPP−, and respective damping coefficients are obtained and tabulated in Table 2. Note that the $\omega_{LO,IR}$ and ω_p^k are calculated using Eq. (2) and the relation of $\omega_p^k = (\omega_{LPP+}\omega_{LPP-})/\omega_{TO}$, respectively. Nevertheless, both the ω_p^k of each $In_xGa_{1-x}N$ layer increases qualitatively with composition. In particular, ω_p^k of top layer L1 (larger porosity) is noticeably lower than ω_p^k in bottom layer L2 (smaller porosity) for all $In_xGa_{1-x}N$. The contribution of plasmon in L1 is even vanishes for InGaN20 and InGaN40 which possess overall low carrier concentration. This coincidence suggests that the carrier concentration decreases when porosity and pore surfaces increases. The findings are parallel to the reported results [29–31,58].

In principle, distinct reflectance spectral features would be observed if the damping is not large. Aforementioned, porous structure would induced additional Fröhlich modes between the TO and LO phonon modes. Surprisingly, no porosity-induced Fröhlich modes are required to be included in the model structure to obtain a rational fit of the spectra. The absence of the spectral features of Fröhlich modes is due to the large damping constant, which heavily suppress the resonant strengths. The combination of Eq. (2) and Drude relation illustrates that the LPP+

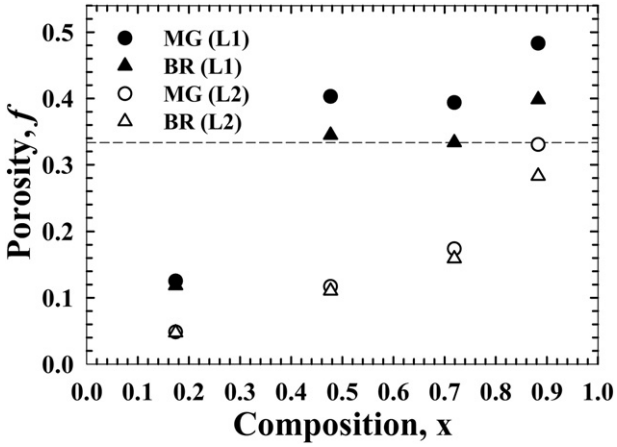

Fig. 4. Comparison between MG calculated and BR calculated porosity of each layers for all $In_xGa_{1-x}N$ samples. The porosity of layer L1 (labeled by filled circle and filled triangle) is higher than layer L2 (labeled by empty circle and empty triangle) for each sample.

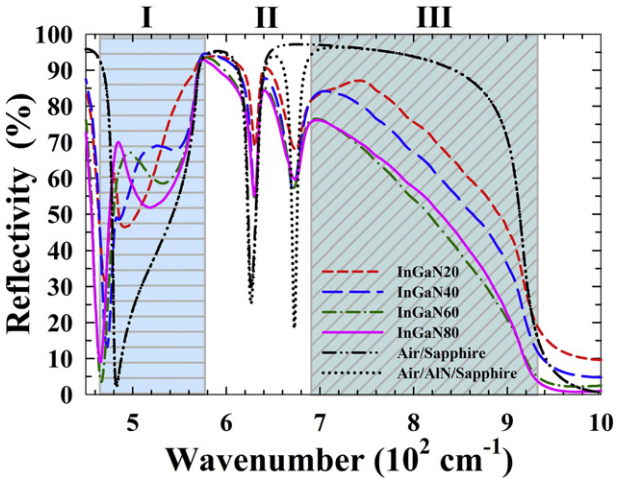

Fig. 5. The peculiarities of experimental IR reflectance spectra of $In_xGa_{1-x}N$ samples. The simulated reflectance spectra of air/sapphire and air/AlN/sapphire are presented in dash-dot-dot line and dotted line respectively.

Table 1
The thickness and high frequency dielectric constant of $In_xGa_{1-x}N$ thin films with different concentration of In content, x determined from the *s*-polarized IR reflectance spectra. L1 denotes to top layer and L2 denotes to bottom layer.

Sample	Composition, x	Layer	Thickness, d (μm)	$d_{L1} + d_{L2}$ (μm)	ε_∞	
					$\varepsilon_{\infty,IR}$	$\varepsilon_{\infty,CM}$
InGaN20	0.174	L1	0.082	0.412	4.80	5.7276
		L2	0.330		5.35	
InGaN40	0.477	L1	0.132	0.332	3.61	6.6746
		L2	0.200		5.61	
InGaN60	0.719	L1	0.189	0.367	4.01	7.4582
		L2	0.178		5.71	
InGaN80	0.883	L1	0.234	0.481	3.63	8.0036
		L2	0.247		4.73	

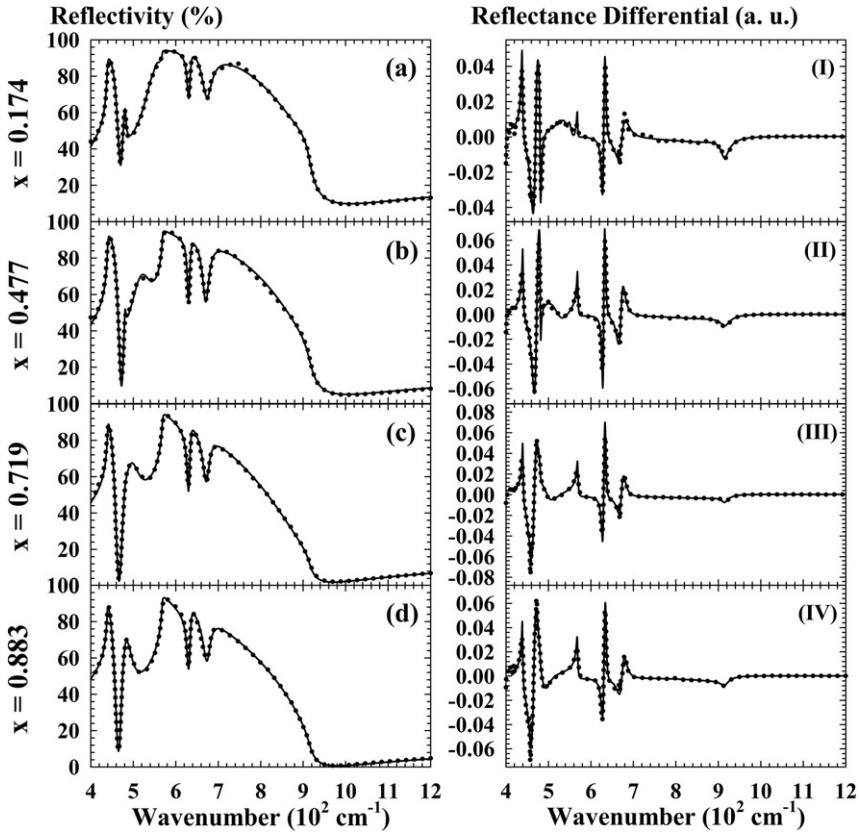

Fig. 6. (a)–(d) Room temperature *s*-polarized IR reflectance spectra and (I)–(IV) the corresponding first derivative spectra of wurtzite $In_xGa_{1-x}N$ thin films with composition x = 0.174, 0.477, 0.719 and 0.883. The dotted (solid) lines refer to experimental (calculated) data.

increases from ω_{LO} to ω_p whereas the LPP− converges from zero to ω_{TO} as carrier concentration increases exponentially. The characteristics of the coupled modes depend on the relation between ω_{LO} and ω_p. If there is no plasmon contribution to the particular oscillator, i.e., $\omega_p = 0$, LOPC does not occur and the LPP+ can be reduced to ω_{LO}. For example, the LPP+ mode is similar to ω_{LO} for L1 of InGaN20 and L1 of InGaN40. For the layer which possesses $\omega_{LO,IR} \gg \omega_p^k$ as indicated by '*' in Table 2, its LPP+ exhibits LO-like behaviour while LPP− behaves plasmon-like. On the other hand, the LPP+ is plasmon-like whereas LPP− is TO-like when $\omega_p^k \gg \omega_{LO,IR}$, as the case of L2 in both InGaN60 and InGaN80 which marked by '#'. If the ω_p^k is comparable to $\omega_{LO,IR}$, the coupled modes exhibit intermediate plasmon-phonon behaviour.

The calculated (MREI) and measured (IR reflectance) E_1 optical phonon modes are summarized in Fig. 7. Overall, the predicted TO phonon are in good agreement with the experimental data (except for InGaN 60 which deviation is about 13 cm^{-1}) as compared to that of the LO phonon. Very often, the deviation of the optical phonon modes between the ideal value and measured values are related to the strain, thermal expansion and anharmonic phonon-coupling [59,60]. At temperature *T*, the IR optical phonon mode $\omega(T)$ is given by [59]:

$$\omega(T) = \omega_0 + \Delta\omega_s(T) + \Delta\omega_e(T) + \Delta\omega_d(T), \tag{11}$$

where ω_0 is the harmonic frequency of the phonon mode, namely, the calculated values of E_1 $\omega_{TO,MREI}$ and $\omega_{LO,MREI}$ in MREI model. $\Delta\omega_s$, $\Delta\omega_e$, and $\Delta\omega_d$ are the phonon mode shift due to residual strain, thermal expansion and anharmonic coupling to phonons of other branches, respectively. The variation of $\Delta\omega_{TO}$ ($\Delta\omega_{TO} = \omega_{TO,IR} - \omega_{TO,MREI}$) is random. The TO phonon mode shift is ascribed to the negligence of temperature-dependent effects. For the biaxial-strained system, $\Delta\omega_s$ can be calculated using $\Delta\omega_s = 2a_{PDP}\epsilon_{xx} + b_{PDP}\epsilon_{zz}$, with a_{PDP} and b_{PDP} are the phonon deformation potential of each mode. The values of a_{PDP} and b_{PDP} for E_1(TO) are

Table 2
Optical parameters determined from the curve fitting of *s*-polarized IR reflectance spectra of wurtzite $In_xGa_{1-x}N$ thin films. The unit for all parameters is cm^{-1}, except for T+ and T−, which refer to the mode behavior of LPP− and LPP+ respectively.

Samples	L	$\omega_{TO,IR}$	γ_{TO}	$\omega_{LO,IR}$	ω_p^k	γ_p^k	ω_{LPP-}	γ_{LPP-}	T_-	ω_{LPP+}	γ_{LPP+}	T_+
InGaN20	L1	549.8	12.5	716.2	–	–	–	–	–	716.2	2.0	LO
	L2*		10.2		202.0	323.0	152.5	329.8	P	728.3	46.0	LO
InGaN40	L1	519.0	26.2	655.4	–	–	–	–	–	655.4	9.96	LO
	L2*		22.5		380.9	431.5	280.7	399.5	P	704.2	131.1	LO
InGaN60	L1*	492.8	18.4	600.0	308.6	109.7	241.4	150.5	P	630.1	15.6	LO
	L2#		24.0		811.4	623.3	440.0	171.3	TO	908.2	490.2	P
InGaN80	L1*	482.0	17.0	540.0	352.7	278.7	296.9	190.4	P	572.6	45.5	LO
	L2#		9.45		948.7	436.1	462.4	83.5	TO	988.8	370.9	P

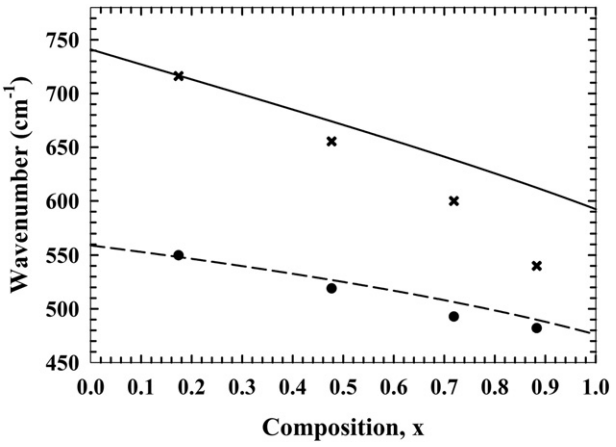

Fig. 7. E_1 optical phonon modes of wurtzite $In_xGa_{1-x}N$. The dashed line and solid line represent the calculated spectra of $\omega_{TO,MREI}$ and $\omega_{LO,MREI}$, respectively. The symbols dot and cross refer to measured E_1 $\omega_{TO,IR}$ and $\omega_{LO,IR}$, respectively.

taken from Ref. [61] (InN) and Ref. [62] (GaN). The expression of $\Delta\omega_e$ is given by:

$$\Delta\omega_e(T = 300K) = -\omega_0\gamma_G \int_0^{T=300K} \left[\alpha_c\left(T'\right) + 2\alpha_a(T')\right] dT', \quad (12)$$

γ_G denotes to Grüneisen parameter. α_c(T) and α_a(T) represents the temperature dependent thermal expansion coefficient parallel and perpendicular the *c*-axis, respectively. The relevant parameters to calculate α_c(T) and α_a(T) for E_1(TO) mode are adopted from reported works [60,63–65]. For simplicity, linear extrapolation technique is employed to obtain the value of the parameters involved in E_1(TO) mode shift calculation, i.e., $\Delta\omega_s$ and $\Delta\omega_e$ for $In_xGa_{1-x}N$. Lastly, the contribution of anharmonic coupling of phonons is calculated. Note that Table 3 is only used to illustrate the contribution of each term qualitatively. The accuracies of $\Delta\omega_s$, $\Delta\omega_e$ and $\Delta\omega_d$ depend on the appropriateness of the linearity assumption and the reliability of the reported parameters used in the calculations.

From Table 3, it is noted that the transition from compressive to tensile in-plane strain occurs with increasing x. The compression typically results in blueshift of optical phonon mode. Vice versa, the tensile strain results in redshift of optical phonon mode as long as the contributions from thermal expansion and anharmonic coupling do not compensate the strain-induced shift. Among all, the contribution of strain for InGaN20 is the largest. Nevertheless, small upshift of $\omega_{TO,IR}$ suggested that the summation of the $\Delta\omega_e$ and $\Delta\omega_d$ nearly acts as an offset to $\Delta\omega_s$. As seen in Fig. 7, the measured $\omega_{TO,IR}$ of InGaN40, InGaN60 and InGaN80 is lower than the predicted harmonic frequency $\omega_{TO,MREI}$. The downshift of InGaN40 and InGaN60 is mainly stemmed from the contribution of anharmonic coupling of phonons whereas the redshift of InGaN80 is mainly attributed to the tensile in-plane strain.

The discrepancy between $\omega_{LO,IR}$ and $\omega_{LO,MREI}$ increases markedly with composition. However, it is unlikely stemmed from the mere temperature effect as the largest deviation approximately up to 70 cm^{-1} is reached for E_1(LO). There is no doubt that the deviation is associated to damping-free derivation of $\omega_{LO,IR}$. In other words, the $\omega_{LO,IR}$ which is calculated from ideal system, is a crude estimation from the practical measurement. As carrier concentration increases, the strengthen LOPC effect reduce the accuracy in retrieving the uncoupled E_1(LO).

Table 3
ϵ_{xx}, ϵ_{zz} and E_1(TO) phonon mode shift due to residual strain ($\Delta\omega_s$), thermal expansion ($\Delta\omega_e$) and anharmonic coupling ($\Delta\omega_d$).

Samples	ϵ_{xx} (%)	ϵ_{zz} (%)	$\Delta\omega_s$ (cm^{-1})	$\Delta\omega_e$ (cm^{-1})	$\Delta\omega_d$ (cm^{-1})
InGaN20	−0.4810	0.1634	6.7648	−2.0866	−3.0382
InGaN40	−0.1033	0.0964	0.9324	−2.0684	−6.5640
InGaN60	0.1162	0.1612	−2.9493	−2.0360	−8.4347
InGaN80	0.2971	0.1826	−5.7438	−2.0010	0.0048

5. Conclusion

In summary, room temperature IR reflectance spectra of unintentionally doped n-type wurtzite $In_xGa_{1-x}N$ ($0.174 \le x \le 0.883$) thin films with porous surface morphology were examined. It was found that the deviation of high frequency dielectric constant, ε_∞ ($\Delta\varepsilon_\infty = \varepsilon_{\infty,ideal} - \varepsilon_{\infty,IR}$) increases with the porosity. Thus, the drop of $\varepsilon_{\infty,IR}$ can be used as an indicator to study the surface morphology. The E_1 phonon modes of wurtzite $In_xGa_{1-x}N$ were investigated thoroughly. The residual strain, thermal expansion and phonon coupling are the three main factors that account for the IR measured E_1(TO) phonon mode shift from predicted harmonic frequency. The behaviour of LPP modes at which the carrier concentration increases with the composition was discussed. As the carrier concentration increases, the accuracy in the determination of uncoupled E_1(LO) is severely obscured by the strengthen LOPC effect.

Acknowledgment

This work was supported by the Ministry of Higher Education of Malaysia through the Fundamental Research Grant Scheme (Grant No. 203/PFIZIK/6711282). The first author would like to acknowledge the Ministry of Higher Education Malaysia for MyBrainSc scholarship.

References

[1] New Light to Illuminate the World, the Nobel Prize in 2014, http://www.nobelprize.org/nobel_prizes/physics/laureates/2014/press.html 2014 (accessed 12 May 2015).
[2] T. Luo, J. Garg, J. Shiomi, K. Esfarjani, G. Chen, Europhys. Lett. 101 (2013) 16001.
[3] Z. Tian, J. Garg, K. Esfarjani, T. Shiga, J. Shiomi, G. Chen, Phys. Rev. B 85 (2012) 184303.
[4] J. Liberis, I. Matulionienė, A. Matulionis, E. Šermukšnis, J. Xie, J.H. Leach, H. Morkoç, Phys. Status Solidi A 206 (2009) 1385–1395.
[5] V.Y. Davydov, A.A. Klochikhin, V.V. Emtsev, A.N. Smirnov, I.N. Goncharuk, A.V. Sakharov, D.A. Kurdyukov, M.V. Baidakova, V.A. Vekshin, S.V. Ivanov, J. Aderhold, J. Graul, A. Hashimoto, A. Yamamoto, Phys. Status Solidi B 240 (2003) 425–428.
[6] S. Hernández, R. Cuscó, D. Pastor, L. Artús, K.P. O'Donnell, R.W. Martin, I.M. Watson, Y. Nanishi, E. Calleja, J. Appl. Phys. 98 (2005) 013511.
[7] R. Oliva, J. Ibáñez, R. Cuscó, R. Kudrawiec, J. Serafinczuk, O. Martínez, J. Jiménez, M. Henini, C. Boney, A. Bensaoula, L. Artús, J. Appl. Phys. 111 (2012) 063502.
[8] M.R. Correia, S. Pereira, E. Pereira, J. Frandon, E. Alves, Appl. Phys. Lett. 83 (2003) 4761–4763.
[9] J.W. Ager III, W. Walukiewicz, W. Shan, K.M. Yu, S.X. Li, E.E. Haller, H. Lu, W.J. Schaff, Phys. Rev. B 72 (2005) 155204.
[10] J.F. Kong, W.Z. Shen, Q.X. Guo, Phys. Status Solidi B 250 (2013) 329–333.
[11] A. Kasic, M. Schubert, J. Off, B. Kuhn, F. Scholz, S. Einfeldt, T. Böttcher, D. Hommel, D.J. As, U. Köhler, A. Dadgar, A. Krost, Y. Saito, Y. Nanishi, M.R. Correia, S. Pereira, V. Darakchieva, B. Monemar, H. Amano, I. Akasaki, G. Wagner, Phys. Status Solidi C 6 (2003) 1750–1769.
[12] T.R. Yang, M.M. Dvoynenko, Y.F. Cheng, Z.C. Feng, Physica B 324 (2002) 268–278.
[13] K. Osamura, S. Naka, Y. Murakami, J. Appl. Phys. 46 (1975) 3432.
[14] A.G. Kontos, Y.S. Raptis, N.T. Pelekanos, A. Georgakilas, E.B. Amalric, D. Jalabert, Phys. Rev. B 72 (2005) 155336.
[15] T. Yuasa, S. Naritsuka, M. Mannoh, K. Shinozaki, K. Yamanaka, Y. Nomura, M. Mihara, M. Ishii, Phys. Rev. B 33 (1986) 1222–1232.
[16] F. Demangeot, C. Pinquier, J. Frandon, M. Gaio, O. Briot, B. Maleyre, S. Ruffenach, B. Gil, Phys. Rev. B 71 (2005) 104305.
[17] M. Chafai, A. Jaouhari, A. Torres, R. Antón, E. Martın, J. Jimenez, W. Mitchel, J. Appl. Phys. 90 (2001) 5211–5215.
[18] A. Kasic, M. Schubert, Y. Saito, Y. Nanishi, G. Wagner, Phys. Rev. B 65 (2002) 115206.
[19] K. Narita, Y. Hijikata, H. Yaguchi, S. Yoshida, S. Nakashima, Jpn. J. Appl. Phys. 43 (2004) 5151–5156.
[20] R. Cuscó, L. Artús, S. Hernández, J. Ibáñez, M. Hopkinson, Phys. Rev. B 65 (2001) 035210.
[21] S. Nakashima, H. Harima, J. Appl. Phys. 95 (2004) 3541–3546.
[22] J.S. Thakur, A. Dixit, Y.V. Danylyuk, C. Sudakar, V.M. Naik, W.J. Schaff, R. Naik, Appl. Phys. Lett. 96 (2010) 181904.
[23] L.R. Bailey, T.D. Veal, P.D.C. King, C.F. McConville, J. Pereiro, J. Grandal, M.A.S. García, E. Muñoz, E. Calleja, J. Appl. Phys. 104 (2008) 113716.
[24] P.D.C. King, T.D. Veal, Hai Lu, P.H. Jefferson, S.A. Hatfield, W.J. Schaff, C.F. McConville, Phys. Status Solidi B 245 (2008) 881–883.
[25] S.F. Cheah, S.C. Lee, S.S. Ng, F.K. Yam, H. Abu Hassan, Z. Hassan, Appl. Phys. Lett. 102 (2013) 101601.

[26] G. Irmer, E. Monaico, I.M. Tiginyanu, G. Gärtner, V.V. Ursaki, G.V. Kolibaba, D.D. Nedeoglo, J. Phys. D. Appl. Phys. 42 (2009) 045405.
[27] C.F. Lin, K.T. Chen, C.M. Lin, C.C. Yang, Electron Device Lett. 30 (2009) 1057–1059.
[28] A. Sarua, J. Monecke, G. Irmer, I.M. Tiginyanu, G. Gärtner, H.L. Hartnagel, J. Phys. Condens. Matter 13 (2001) 6687–6706.
[29] P.A. Ivanov, M.G. Mynbaeva, S.E. Saddow, Semicond. Sci. Technol. 19 (2004) 319–322.
[30] D.C. Look, Z.Q. Fang, S. Soloviev, T.S. Sudarshan, J.J. Boeckl, Phys. Rev. B 69 (2004) 195205.
[31] S. Soloviev, T. Das, T.S. Sudarshan, Electrochem. Solid-State Lett. 6 (2003) G22–G24.
[32] J.A. Maxwell, J.L. Campbell, W.J. Teesdale, The Guelph PIXE software package, Nucl. Instrum. Methods B 43 (1989) 218–230.
[33] V. Darakchieva, T. Paskova, M. Schubert, H. Arwin, P.P. Paskov, B. Monemar, D. Hommel, M. Heuken, J. Off, F. Scholz, B.A. Haskell, P.T. Fini, J.S. Speck, S. Nakamura, Phys. Rev. B 75 (2007) 195217.
[34] T. Dumelow, T.J. Parker, S.R.P. Smith, D.R. Tilley, Surf. Sci. Rep. 17 (1993) 151.
[35] F. Gervais, B. Piriou, J. Phys. C Solid State Phys. 7 (1974) 2374–2386.
[36] R.E. Kroon, Infrared Phys. Technol. 51 (2007) 31–43.
[37] C.M. Wolfe, N. Holonyak, G.E. Stillman, Physical Properties of Semiconductors, first ed. Prentice-Hall, Inc., 1988.
[38] A.A. Kukharskii, Solid State Commun. 13 (1973) 1761–1765.
[39] S. Perkowitz, R.H. Thorland, Solid State Commun. 16 (1975) 1093–1096.
[40] I.F. Chang, S.S. Mitra, Phys. Rev. 172 (1968) 924–933.
[41] L. Genzel, T.P. Martin, C.H. Perry, Phys. Status Solidi B 62 (1974) 83–92.
[42] S. Yu, K.W. Kim, L. Bergman, M. Dutta, M.A. Stroscio, J.M. Zavada, Phys. Rev. B 58 (1998) 15283–15287.
[43] H.W. Verleur, A.S. Barker Jr., Phys. Rev. 164 (1967) 1169–1184.
[44] M.A. Moram, M.E. Vickers, Rep. Prog. Phys. 72 (2009) 036502.
[45] T. Yang, S. Goto, M. Kawata, K. Uchida, A. Niwa, J. Gotoh, Jpn. J. Appl. Phys. 37 (1998) L1105–L1108.
[46] B.E. Foutz, S.K. O'Leary, M.S. Shur, L.F. Eastman, J. Appl. Phys. 85 (1999) 7727–7734.
[47] V.Y. Davydov, Y.E. Kitaev, I.N. Goncharuk, A.N. Smirnov, J. Graul, O. Semchinova, D. Uffmann, M.B. Smirnov, A.P. Mirgorodsky, R.A. Evarestov, Phys. Rev. B 58 (1998) 12899–12907.
[48] V.Y. Davydov, V.V. Emtsev, I.N. Goncharuk, A.N. Smirnov, V.D. Petrikov, V.V. Mamutin, V.A. Vekshin, S.V. Ivanov, M.B. Smirnov, T. Inushima, Appl. Phys. Lett. 75 (1999) 3297–3299.
[49] H. Grille, C. Schnittler, F. Bechstedt, Phys. Rev. B 61 (2000) 6091–6105.
[50] S.G. Moiseev, Physica B 405 (2010) 3042–3045.
[51] J.J. Saarinen, S.M. Weiss, P.M. Fauchet, J.E. Sipe, J. Appl. Phys. 104 (2008) 013103.
[52] S.N. Volkov, J.J. Saarinen, J.E. Sipe, J. Mod. Opt. 59 (2012) 954–961.
[53] I. Webman, J. Jortner, M.H. Cohen, Phys. Rev. B 15 (1977) 5712–5723.
[54] G. Durkaya, M. Buegler, R. Atalay, I. Senevirathna, M. Alevli, O. Hitzemann, M. Kaiser, R. Kirste, A. Hoffmann, N. Dietz, Phys. Status Solidi A 207 (2010) 1379–1382.
[55] T.R. Barlas, N.L. Dmitruk, V.A. Serdyuk, Opt. Spectrosc. 112 (2012) 233–242.
[56] C.G. Granqvist, O. Hunderi, Phys. Rev. B 18 (1978) 2897–2906.
[57] J.E. Spanier, I.P. Herman, Phys. Rev. B 61 (2000) 10437–10450.
[58] M. Mynbaeva, N. Bazhenov, K. Mynbaev, V. Evstropov, S.E. Saddow, Y. Koshka, Y. Melnik, Phys. Status Solidi B 228 (2001) 589–592.
[59] A. Link, K. Bitzer, W. Limmer, R. Sauer, C. Kirchner, V. Schwegler, M. Kamp, D.G. Ebling, K.W. Benz, J. Appl. Phys. 86 (1999) 6256–6260.
[60] X.D. Pu, J. Chen, W.Z. Shen, H. Ogawa, Q.X. Guo, J. Appl. Phys. 98 (2005) 033527.
[61] V. Darakchieva, P.P. Paskov, E. Valcheva, T. Paskova, B. Monemar, M. Schubert, H. Lu, W.J. Schaff, Appl. Phys. Lett. 84 (2004) 3636–3638.
[62] G. Callsen, J.S. Reparaz, M.R. Wagner, R. Kirste, C. Nenstiel, A. Hoffmann, M.R. Phillips, Appl. Phys. Lett. 98 (2011) 061906.
[63] A.R. Goñi, H. Siegle, K. Syassen, C. Thomsen, J.M. Wagner, Phys. Rev. B 64 (2001) 035205.
[64] J. Ibáñez, F.J. Manjón, A. Segura, R. Oliva, R. Cuscó, R. Vilaplana, T. Yamaguchi, Y. Nanishi, L. Artús, Appl. Phys. Lett. 99 (2011) 011908.
[65] H. Iwanaga, A. Kunishige, S. Takeuchi, J. Mater. Sci. 35 (2000) 2451–2454.